Journal of
Materials Chemistry A

Accepted Manuscript

This article can be cited before page numbers have been issued, to do this please use: R. O. Fuentes, L. M. Acuña, A. G. Leyva, R. Baker, H. Pan, X. Chen and J. J. Delgado, *J. Mater. Chem. A*, 2018, DOI: 10.1039/C8TA00203G.

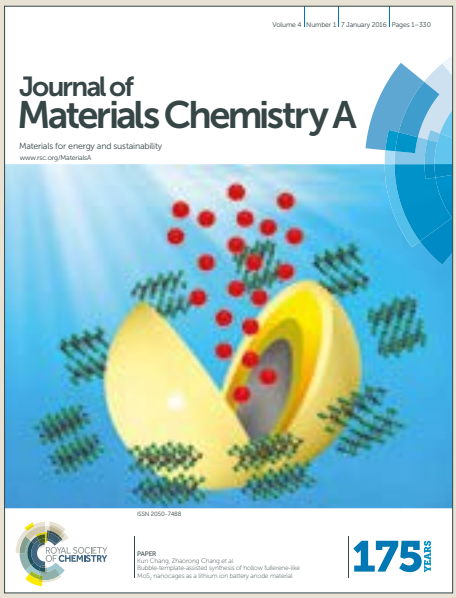

ROYAL SOCIETY OF CHEMISTRY

rsc.li/materials-a

View Article Online
DOI: 10.1039/C8TA00203G

Journal Name

ARTICLE

Physicochemical properties of nanostructured Pd/lanthanide-doped ceria spheres with high catalytic activity for CH_4 combustion

Received 00th January 20xx,
Accepted 00th January 20xx

DOI: 10.1039/x0xx00000x

www.rsc.org/

Rodolfo O. Fuentes,[*a, b] Leandro M. Acuña,[b,c] A. Gabriela Leyva,[a,d] Richard T. Baker,[e] Huiyan Pan,[f] Xiaowei Chen[f] and Juan J. Delgado-Jaén[f]

In this work, nanostructured $Ce_{0.9}Gd_{0.1}O_{2-\delta}$ (GDC) and $Ce_{0.9}Pr_{0.1}O_{2-\delta}$ (PrDC) spheres previously obtained by microwave assisted hydrothermal homogeneous co-precipitation were impregnated with 1 wt% Pd by the incipient wetness impregnation of an aqueous Pd^{2+} solution. Their properties were characterized by synchrotron radiation X-ray diffraction (SR-XRD), X-ray absorption near-edge spectroscopy (XANES) and scanning and high resolution electron microscopy with X-ray spectroscopy. Spherical particles with average diameters around 200 nm were found to consist of crystallites of average size, 10 nm, with small particles of PdO finely dispersed over the sphere surface. *In situ* XRD and XANES experiments were carried out under reducing and oxidizing conditions in order to investigate the redox behaviour of these materials and to evaluate the effect of Pd loading on the oxidation state of Ce. All of the lanthanide-doped ceria (LnDC) supports were found to have a cubic crystal structure (Fm3m space group). An increase in lattice parameters was observed under reducing conditions which was attributed to the reduction of Ce^{4+} ions to the larger Ce^{3+} ions, and to the associated increase in oxygen vacancy (V_O) concentration. Addition of Pd to the LnDC spheres increased their Ce^{3+} content. Finally, catalytic tests for CH_4 combustion were performed on the LnDC and Pd/LnDC nanocatalysts. The best performance was observed in samples with 1 wt% Pd loading, which exhibited T_{50} values (temperature at which 50% of CH_4 conversion was reached) close to 310 °C. These values are 220 °C and 260 °C lower than those obtained for nanostructured PrDC and GDC spheres alone, respectively.

Introduction

Their applications, such as in three-way catalysts, oxygen gas sensors and electrodes and electrolytes for solid oxide fuel cells, mean that ceria-based mixed oxides are materials with a large technological impact, especially in the area of environmental protection.[1-4] A vast range of catalytic applications make use of the reversible oxygen storage ability of ceria-based materials, a phenomenon which is closely connected to the Ce^{4+}/Ce^{3+} redox couple.[5]

Many of these applications rely on the high oxygen ion conductivity and oxygen storage capacity which can easily be achieved in ceria by doping with other aliovalent cations, such as rare earth elements (e.g. Gd, Pr, Tb). This creates oxygen vacancies which enable migration of oxygen ions through the lattice.[6-8]

Under reducing atmospheres, both electronic (Ce'_{Ce}) and ionic ($V_O^{\bullet\bullet}$) charge carriers can be created through loss of oxygen ions from the lattice as molecular oxygen. The presence of both types of charge carriers gives rise to mixed (ionic and electronic) conducting behaviour in both undoped and doped cerias (e.g. Lanthanide-doped cerias, LnDCs) under reducing conditions. This is a difficulty for the application of LnDCs in SOFC electrolytes - where electronic conductivity would give rise to an internal short circuit of the electrolyte - but would be an advantage for the use of these doped cerias in anodes for IT-SOFCs. For example, the use Gd-Doped Ceria in anode materials in intermediate temperature (IT)-SOFCs has been proposed in several studies in this and related areas, especially on its use as a catalyst support.[9,10] This increasing use of

[a] Instituto de Nanociencia y Nanotecnología Departamento de Física, Centro Atómico Constituyentes, CNEA, Av. Gral. Paz 1499, (1650) San Martín, Buenos Aires, Argentina.
[b] CONICET, Buenos Aires, Argentina.
[c] DEINSO (Departamento de Investigaciones en Sólidos), UNIDEF-CITEDEF, J.B. de la Salle 4397, (1603) Villa Martelli, Buenos Aires, Argentina..
[d] Escuela de Ciencia y Tecnología, Universidad Nacional de San Martín, M de Yrigoyen3100, (1650) San Martín, Buenos Aires, Argentina.
[e] 5EaStChem, School of Chemistry, University of St. Andrews, North Haugh, St. Andrews, Fife, KY16 9ST, United Kingdom.
[f] Departamento de Ciencia de los Materiales e Ingeniería Metalúrgica y Química Inorgánica, Universidad de Cádiz, Campus Río San Pedro, Puerto Real, Cádiz, Spain.
* Corresponding author e-mail: rofuentes@conicet.gov.ar.

Electronic Supplementary Information (ESI) available: Elemental profiles and electron image (HAADF) and corresponding distribution maps for the elements of nanostructured 1 wt% Pd/PrDC spheres are presented in Fig. S1 and S2, SR-XRD patterns recorded at 500 °C in different atmospheric conditions for nanostructured 1 wt% Pd/LnDC spheres are given in Fig. S3-S7 and their corresponding structural parameters and standard Rietveld agreement factors are presented in Tables S1 and S2. The catalytic performance (obtained by eq. 1) over the catalysts for CH_4 oxidation reported in the literature is presented in Table S3 and Results of cyclic catalytic stability performed in 1 wt% Pd/LnDC spherical nanocatalysts are presented in Fig S8-S10 and Tables S4-S5.]. See DOI: 10.1039/x0xx00000x

such materials as catalyst and fuel cell components has prompted a renewed interest in their preparation in the form of nanostructured materials with controlled morphologies and high surface areas.

Hydrocarbons are proposed as fuels for SOFCs. Among the hydrocarbons, methane (CH_4), being the main component of natural gas, is of particular importance. Direct, electrochemical conversion of methane in a fuel cell would represent a significant improvement in efficiency, and so a dramatic reduction in CO_2 production, compared with conventional methane combustion, for electricity generation.[11-14]

In recent years, substantial progress in the controlled synthesis and catalytic applications of ceria-based nanocatalysts has been reported. Recent developments of ceria-based nanomaterials have paid particular attention to the general synthetic strategies and to the control of morphology, surface defects and composition. These investigations were focused on design and application of novel, highly efficient nanoceria catalysts for practical applications such as CO oxidation, preferential oxidation of CO (PROX) and the water-gas-shift (WGS) reaction as well as other energy-related applications in SOFCs, proton exchange membrane fuel cells (PEMFCs), and photocatalytic and catalysed organic reactions.[15]

In order to improve methane oxidation catalysts, a supramolecular approach has been reported in which single units composed of a palladium (Pd) core and a ceria (CeO_2) shell are preorganized in solution and then homogeneously deposited onto a modified hydrophobic alumina.[16] Enhanced metal-support interactions led to exceptionally high methane oxidation activity, with complete combustion below 400°C and outstanding thermal stability under demanding conditions. Recently, S. Xie et al. reported the high activity of three-dimensionally ordered macroporous CeO_2-supported Pd@Co nanoparticles for methane oxidation. The excellent catalytic performance was associated with their ability to adsorb oxygen and methane as well as with the unique core-shell structure of the Co@Pd nanoparticles. [17]

In a previous study, the authors reported on the synthesis and catalytic properties of nanostructured 1 wt% Pd/$Ce_{0.9}Gd_{0.1}O_{2-\delta}$ tubes.[18] Results suggested that Pd cations, most likely Pd^{2+}, formed a Pd-Ce-Gd oxide solid solution and that the Pd^{2+} was stabilized against reduction in this phase. However, incorporation of the Pd (1 wt%) into the crystal lattice of the nanostructured tubes also appeared to destabilize Ce^{4+}, favoring reduction to Ce^{3+} and giving rise to a significant increase in the reducibility of this material. Preliminary catalytic studies showed a slightly improved catalytic activity toward CH_4 oxidation compared to pure $Ce_{0.9}Gd_{0.1}O_{2-\delta}$ (either nanotubes or nanopowders). In subsequent work, the authors reported the catalytic properties of 1 and 5 wt% Pd/$Gd_{0.1}Ce_{0.9}O_{2-\delta}$ nanopowders prepared by two different methods (cation complexation and incipient wetness impregnation of an aqueous Pd^{2+} solution into $Ce_{0.9}Gd_{0.1}O_{2-\delta}$ nanopowders).[19] Catalysts with the higher Pd loading (5 wt%) exhibited the best performance for CH_4 combustion. The influence of preparation method was evident for catalysts with 1 wt% Pd, cation complexation resulting in more active catalysts than the wetness impregnation method, mainly due to the differences in Pd distribution.

The main objective of the present study is to focus on the correlation between structural, redox and catalytic properties of Pd supported on nanostructured ceria materials with a controlled morphology and doped with either a univalent (Gd^{3+}) or a multivalent ($Pr^{3+,4+}$) cation. In the present work, nanostructured $Ce_{0.9}Gd_{0.1}O_{2-\delta}$ (GDC) and $Ce_{0.9}Pr_{0.1}O_{2-\delta}$ (PrDC) spheres previously obtained by microwave assisted hydrothermal homogeneous co-precipitation (HMW), as reported by Muñoz *et al.*, [20] were impregnated with 1 wt% Pd by incipient wetness impregnation (WI) of an aqueous Pd^{2+} solution. The resulting samples, Pd/LnDC (1 wt% Pd/GDC and 1 wt% Pd/PrDC), were characterized by synchrotron radiation X-ray diffraction (SR-XRD), X-ray absorption near-edge spectroscopy (XANES), extended X-ray absorption fine structure (EXAFS), scanning and high resolution transmission electron microscopy (SEM and HRTEM) and energy dispersive X-ray spectroscopy (EDS). The redox properties of the materials were studied using *in situ* XAS (XANES) and XRD experiments carried out under reducing and oxidizing atmospheres at temperatures up to 500 °C. Finally, catalytic tests for CH_4 combustion were performed on the Pd/LnDC spherical nanocatalysts.

Experimental

Nanostructured GDC and PrDC spheres were synthesized by HMW.[18] $Ce(NO_3)_3.6H_2O$ (99.99%, Alfa Aesar), $Gd(NO_3)_3.6H_2O$ (99.9%, Alfa Aesar) and $Pr(NO_3)_3.6H_2O$ (99.9%, Alfa Aesar) were employed as precursors. Each nitrate was dissolved in pure deionized H_2O separately and then the solutions were mixed to obtain a 0.1 M nitrate solution with molar ratios of Ce:Gd and Ce:Pr appropriate for the preparation of GDC and PrDC, respectively. Urea was added in order to give a molar ratio of urea:final oxide of 4:1 and 60 ml of the resulting solution was placed in a Teflon-lined autoclave. A Milestone ETHOS 1 Advanced Microwave Digestion system was employed. The sealed autoclave was placed in the oven and was heated to 120 °C with a ramp rate of 30 °C.min^{-1} -with oven power set to 550 W- and then kept at this temperature for 1 h. After cooling, the white powder product was collected by centrifugation (2.5 min at 7830 rpm) and dried at 37 °C for 12 h. After calcination at 500 °C in air for 1 h, the nanostructured LnDC spheres were obtained. These were impregnated with 1wt% Pd by WI of an aqueous $Pd(NO_3)_2$ solution. All resulting catalysts were dried at 100 °C and calcined at 500 °C for 1 h in air, in order to decompose any unreacted nitrate precursor.

In order to verify the phase composition, conventional X-ray diffraction (XRD) was performed in a PANalytical Empyream 2 with a PIXcel^{3D} detector employing Cu-K_α radiation (of wavelength 1.5418 Å). Data in the angular range 2θ = 20 - 90° were collected in step-scanning mode, with a step length of 0.04° and a step-counting time of 4 s. The average crystallite size, D_{XRD}, of the products was determined using the Scherrer formula from the extent of peak broadening of the main XRD

reflection, (111).[19] Errors in crystallite size were derived by estimating the error in the FWHM (full-width at half-maximum) to be equal to the 2θ step.

Nitrogen adsorption-desorption isotherms were obtained using an Autosorb-1 instrument from Quanta chrome. Out gassing was carried out at 200 °C for 16 h prior to the measurements. Analysis of the isotherms using the BET method provided values of the specific surface area (SSA) of the samples.

SEM images were obtained in secondary electron mode using a JEOL 6700F instrument with Field Emission Gun (FEG) and the X-ray spectrometer attached to this microscope was used to record EDS spectra. Values of accelerating voltage (in kV) and working distance (WD) are given in the images. Samples were imaged in the FEG-SEM uncoated.

TEM images were recorded using a JEOL JEM 2011 instrument operating with a LaB_6 filament at an accelerating voltage of 200 kV and equipped with an Oxford Instruments EDS spectrometer. The images were captured using a Gatan CCD camera and analyzed using Digital Micrograph 3.4.4 software. This software was also used to calculate Digital Diffraction Patterns (DDPs) by fast Fourier transform of regions of interest of the TEM images. The image analysis software, ImageJ, was used to obtain particle size information from the TEM images. A Titan Themis 200 keV (FEI) transmission and scanning transmission electron microscope (S/TEM) equipped with an X-FEG Schottky field emission gun and a spherical aberration corrector was employed to obtain electron images in High Angle Angular Dark Field (HAADF) mode. Its Super-X high sensitivity windowless EDS detector was used to generate line scans and two-dimensional maps of the elemental composition of the samples. For TEM examination, the samples were suspended in acetone by ultrasonication and deposited onto holey carbon-coated Cu grids.

XRD patterns were recorded at high temperatures (HT) and in controlled atmospheres using synchrotron radiation at the D10B-XPD beamline of the National Synchrotron Light Laboratory (LNLS, Campinas, Brazil). In these *in situ* XRD experiments, the sample was mounted on a ceramic sample-holder and placed in a furnace. The X-ray wavelength was set at 1.54892 Å. Data in the angular range 2θ = 20 - 100° were collected in step-scanning mode, with a step length of 0.04° and a step-counting time of 2 s. The data were collected at temperatures ranging from room temperature to 500 °C. The sample was heated at a rate of 10 °C/min, and a soak time of 10 min was employed at each temperature step before performing the XRD scan. The thermal and redox behavior of the materials was studied in 5% H_2/He (total flow: 20 ml.min^{-1}) and in dry synthetic air (total flow: 50 ml.min^{-1}). NIST SRM 640c Si powder was used as the standard for the instrumental broadening correction.

In situ XAS (XANES) experiments under conditions of controlled temperature and atmosphere were carried out at the D04B-XAFS1 beamline at LNLS in transmission mode using a Si(111) monochromator for the Ce L_3-edge (5726 eV) and Pr L_3-edge (5960 eV). The nominal photon flux of the beamline is 3x10^9 photons/(s.mrad.100mA)@6keV. All spectra were collected at energies in the range 5690-6100 eV (for the Ce L_3-edge and Pr L_3-edge) with E/ΔE=5000 to 10000. Energies for the Ce L_3-edge and Pr L_3-edge were calibrated using a Cr foil (5989 eV). Two acquisitions were made on the same sample to improve the signal to noise ratio. Samples were diluted with boron nitride and these mixtures were pressed into 15 mm diameter pellets (around 6 mg of sample and 70 mg of diluent were used). For the transmission measurements, the pellets were placed in a tubular quartz furnace (diameter, 20 mm; X-ray path length, 440 mm) sealed with refrigerated Kapton windows. Temperature was measured and controlled by a thermocouple passed down the sample holder and positioned close to the surface of the pellet. Temperature-resolved XAS spectra at the Ce L_3-edge and Pr L_3-edge were acquired during temperature programmed reduction (TPR) under 5% H_2/He (total flow: 20 ml.min^{-1}) at temperatures from 25 to 500 °C at a heating rate of 10 °C.min^{-1} and with a total data acquisition time of 20 min per spectrum. After the data were collected at 500 °C under 5% H_2/He, the system was purged with N_2 (100 ml.min^{-1}) and synthetic air (21% O_2/N_2; total flow: 50 ml.min^{-1}) was passed through the furnace. After 10 min, data were collected under these oxidizing conditions.

Temperature-programmed reduction experiments in hydrogen (H_2-TPR) were carried out using a Quadruple Mass Spectrometer (PrismaPlus® QMA 220 M). Before each TPR measurement, ca. 0.1 g of the sample was loaded into a quartz fixed-bed U-shaped micro reactor and pretreated in 5% O_2/Ar flow of 60 mL/min at 500 °C for 1 h. After cooling in the same atmosphere to 150 °C, the gas was switched to a flow of He and the reactor was cooled to RT. The pretreated sample was exposed to a flow (60 mL. min^{-1}) of a 5% H_2/Ar gas mixture and heated from RT to 900 °C at a ramp rate of 10 °C.min^{-1}.

Catalytic tests were performed in a quartz U-tube reactor equipped with a furnace and temperature controller. All the experiments were carried out with 75 mg of catalyst diluted with 150 mg of SiC. Before methane combustion tests, the samples were pretreated in 20% O_2-Ar gas mixture (60 mL.min^{-1}) at 450 °C for 1 h to remove the water and carbonates adsorbed on the sample surface. After cooling to room temperature, the reactor was purged with pure Ar for 30 minutes to eliminate weakly absorbed O_2. The reaction mixture – of composition: 2.1 mL.min^{-1} of CH_4, 11.6 mL.min^{-1} of O_2 and 61.3 mL.min^{-1} of Ar-was flowed through the reactor at room temperature for 30 min after which the reactor was heated to 900 °C at a ramp rate of 10 °C.min^{-1}. A similar experiment was performed on 150 mg of SiC under the same reaction conditions as a blank experiment. A Quadruple Mass Spectrometer (PrismaPlus® QMA 220 M) was used to collect data on reactant and product concentrations in the gas leaving the reactor. Cyclic catalytic stability tests were performed in the same experimental setup and under the same conditions. Each cycle consisted in increasing the temperature from 125 °C to 500 °C at a ramp rate of 10 °C.min^{-1} and maintaining the system at 500 °C for 2 h. The reaction rates were calculated using the methane signal and the following equation (1):

$$rate = \frac{F_{CH_4} * X_{CH_4}}{100 * W_{Pd}} \quad (1)$$

where F_{CH_4} is the molar flow rate of methane in mmols.min^{-1}, W_{Pd} is the mass of Pd in grams and X_{CH_4} is the methane conversion in percent.

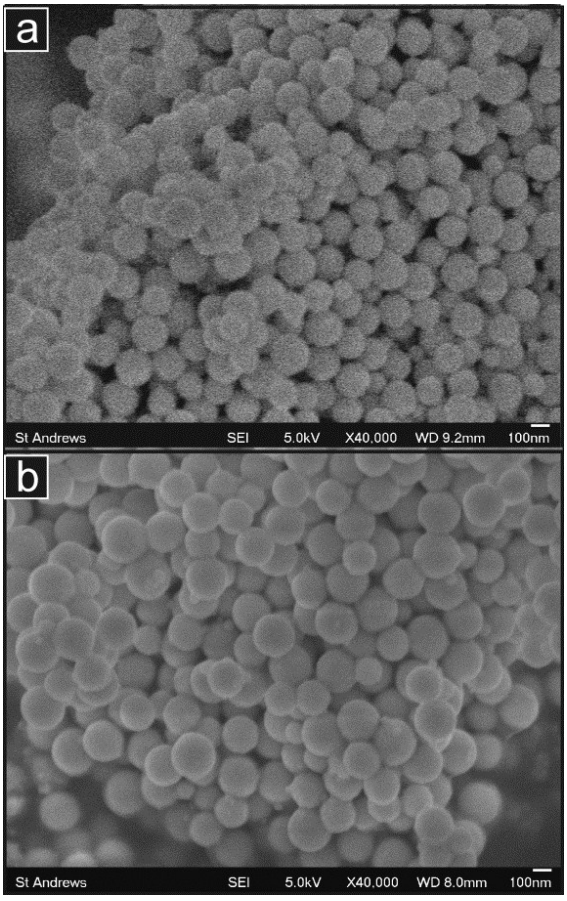

Figure 1. FEG-SEM images of (a) 1wt% Pd/GDC and (b) 1wt% Pd/PrDC samples

Results and discussion

The morphology and chemical compositions of the nanostructured 1 wt% Pd/LnDC spheres were studied by SEM and TEM. The SEM images in **Figure 1** confirmed that both samples showed a very high yield of the expected uniform spherical particles with a narrow size distribution. TEM images at a range of magnifications are presented for 1 wt% Pd/GDC and 1 wt% Pd/PrDC in **Figures 2** and **3**, respectively. Again there is very little extraneous material, the large majority of the particles imaged being regular spheres. These were measured from a number of TEM images and found to have diameters of 205 ± 36 (one standard deviation) nm and 189 ± 24 nm for the 1 wt% Pd/GDC and 1 wt% Pd/PrDC samples, respectively. The contrast variations across the spherical particles in the medium magnification images indicate that these are composed of many much smaller particles. In the high resolution images these are seen to be nanocrystals of around 5-10 nm diameter. For example, the crystallite circled in **Figure 3(d)** can be indexed to the cubic fluorite structure of ceria viewed along the [211] zone axis. The nominal compositions of the GDC and PrDC supports were confirmed by EDS in the SEM and TEM instruments and the presence of the Pd at around 1 wt% was also confirmed

View Article Online DOI: 10.1039/C8TA00207G

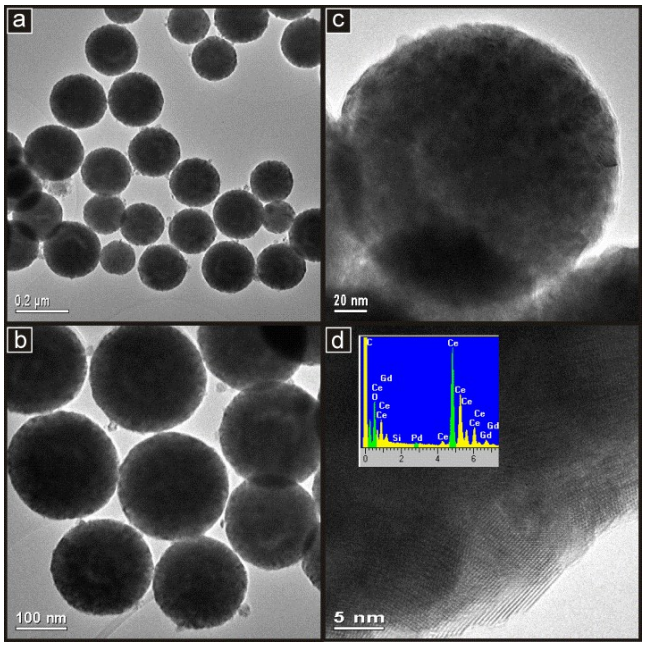

Figure 2. TEM images of 1 wt% Pd/GDC at increasing magnifications (a-d). The partial EDS spectrum inset in (d) is of a large area containing many spherical particles and confirms the presence of Ce, Gd and a small concentration of Pd.

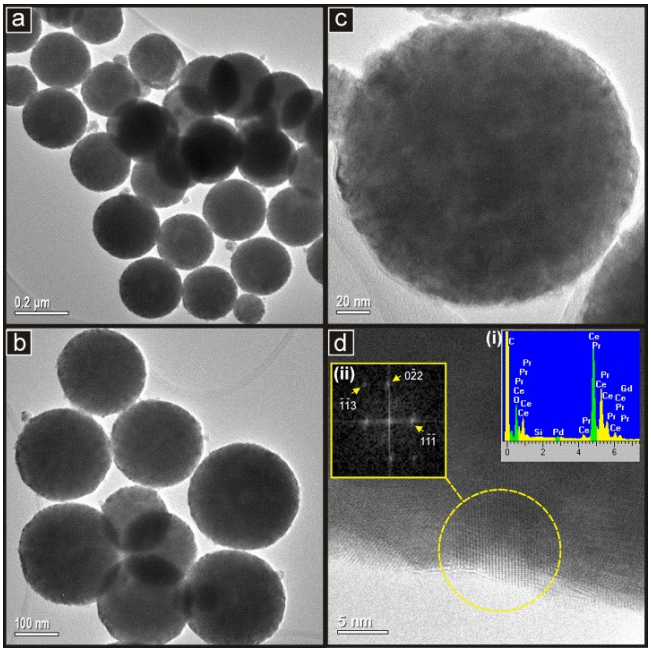

Figure 3. TEM images of 1 wt% Pd/PrDC at increasing magnifications (a-d). The partial EDS spectrum (i) is of a large area containing many spherical particles and confirms the presence of Ce, Pr and a small concentration of Pd. The DDP inset was calculated from the crystallite circled and can be indexed to ceria viewed along the [211] zone axis.

The spatial distributions of the constituent elements of the Pd/GDC material were obtained by recording EDS line scans

and maps such as those presented in **Figure 4** for a group of three spherical particles. These show coincident distributions of Ce, O and Gd, indicating the successful synthesis of the GDC mixed oxide as a single phase. These distributions also match the grayscale variations seen in the HAADF images, which are directly related to sample density. The Pd signals also show that this element is quite evenly distributed through the GDC support material. However, the peaks seen in the Pd traces in the line scans in **Figure 4(b)** and **(d)** indicate that at least a proportion of the Pd is present in the form of discreet Pd-rich nanoparticles of a few nm in diameter. A similar set of maps and line scans are given

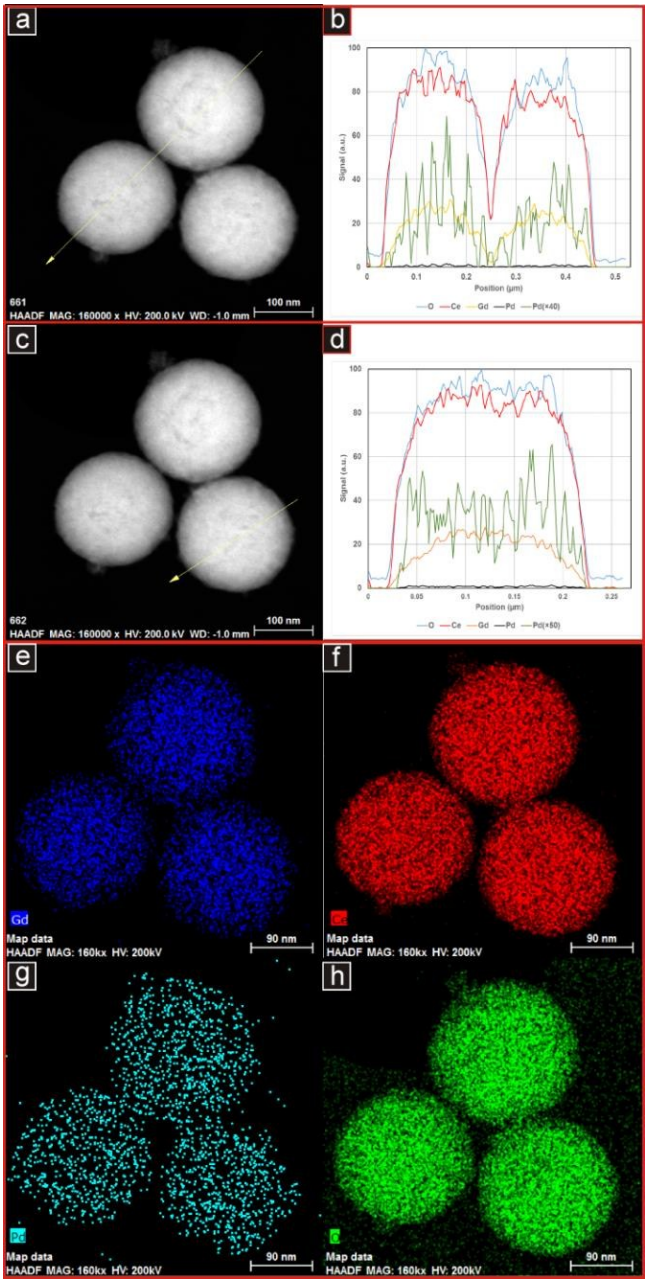

Figure 4. Electron images (HAADF) and corresponding elemental profiles along the lines indicated for two (a, b) and one (c,d) 1 wt% Pd/GDC spheres; distribution maps of the elements Gd (e), Ce (f), Pd (g) and O (h) for the same group of spheres.

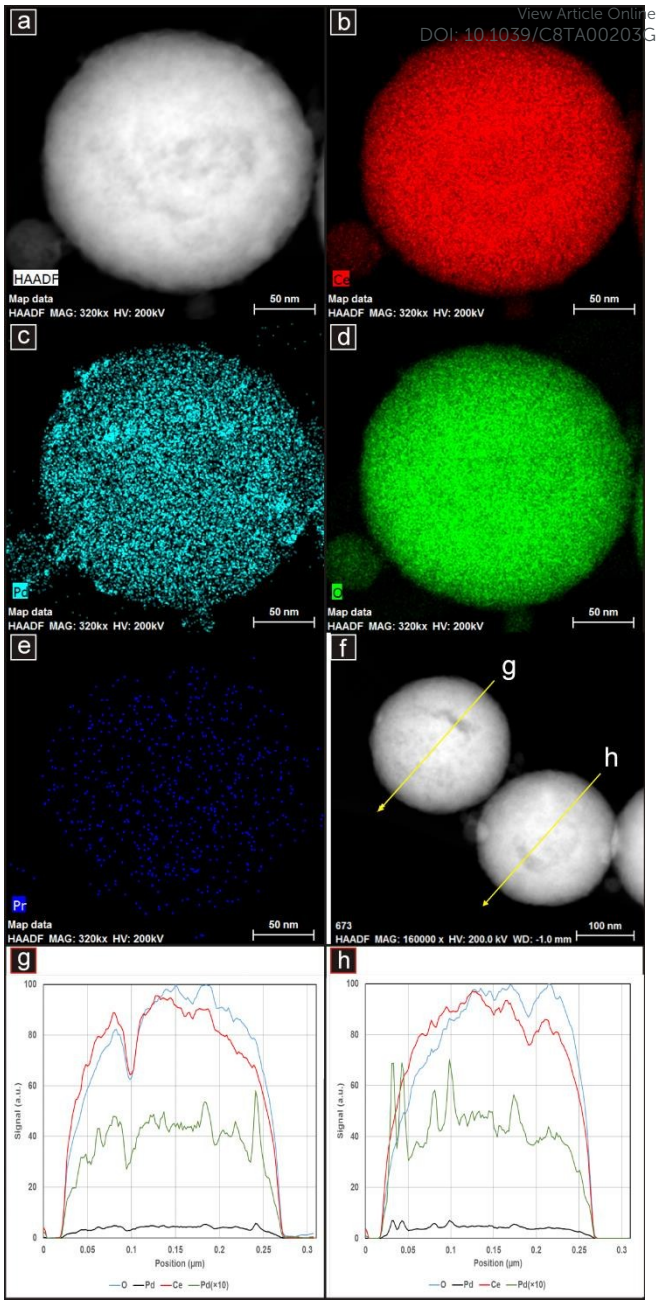

Figure 5. Electron (HAADF) image (a) and corresponding distribution maps of the elements Ce (b), Pd (c), O (d) and Pr (e) in a single Pd/PrDC sphere; HAADF image of two 1 wt% Pd/PrDC spheres (f) with elemental profiles along the lines indicated for each (g,h).

in **Figure 5** for the 1 wt% Pd/PrDC sample. The Ce, O and Pr distributions again closely match with each other as well as with the grayscale variations seen in the HAADF images, confirming that the PrDC single phase has also been formed successfully. The Pr Lα peak overlaps with some Ce peaks so in this figure the Pr Kα peak, which does not overlap but which gives a weaker response, was used to provide a map which is independent of the Ce distribution (**Figure 5(e)**). Again, Pd is present throughout the support material but the localized concentrations of Pd observed in the Pd elemental map (**Figure 5(c)**) and implied in the peaks seen in the line scans

View Article Online
DOI: 10.1039/C8TA00303G

(**Figure 5(g)** and **(h)**) indicate the presence of discreet Pd-rich nanoparticles. This is what would be expected to result from successful impregnation by incipient wetness of the Pd precursor onto previously prepared GDC or PrDC spheres. Further HAADF images, line scans and elemental maps are presented in Figures S1 and S2 in Supplementary Information.

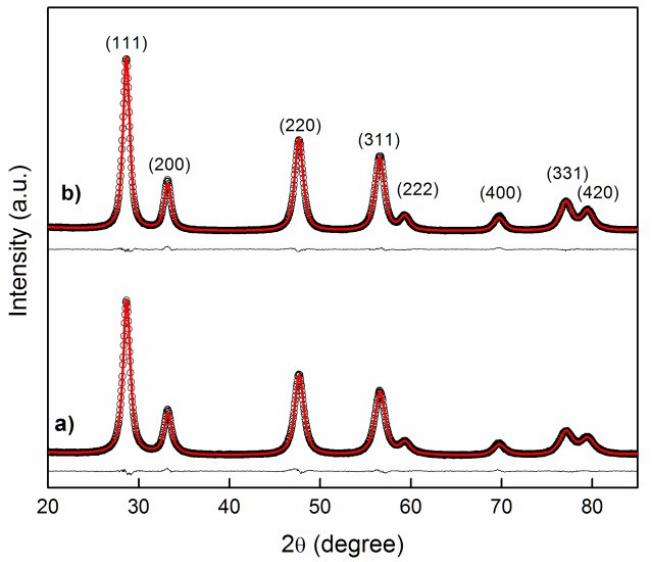

Figure 6. Synchrotron XRD patterns recorded at room temperature (empty circles) with the Rietveld-fitted pattern (red line) and the difference plot for (a) 1 wt% Pd/GDC and (b) Pd/PrDC spheres.

A crystallographic study was performed by Rietveld refinement of the SR-XRD data employing the FullProf suite of software.[22] For the cubic phase, the *Fm*3*m* space group was assumed, with (Gd^{3+}, Pr^{3+}, Ce^{4+}) cations and O^{2-} anions in 4a and 8c positions, respectively. The peak shape was assumed to be a pseudo-Voigt function. The background of each profile was fitted using a six-parameter polynomial function in $(2\theta)^n$, n = 0–5. The thermal parameters were assumed to be equal. A second phase corresponding to PdO (space group $P4_2/mmc$ with Pd^{2+} and O^{2-} in 2d and 2e positions, respectively, according to ICDS#24692), was included. No diffraction lines corresponding to Pd or PdO were observed in the SR-XRD pattern collected at room temperature for 1 wt% Pd/GDC or 1 wt% Pd/PrDC (**Figure 6a** and **b**, respectively). In the same figure, the Rietveld fitted pattern (line) and the difference plot are included. Even a scan with a larger counting time in the regions where the Pd(111) and PdO(111) peaks would be expected did not show any evidence of metallic Pd or PdO. However, a small difference between experimental data and the fitted line close to where the PdO (111) peak would be expected was observed, when the PdO phase is not included in the refinement (see Electronic Supplementary Information, **Fig. S3**). The results of Rietveld refinement of the SR-XRD data are summarized in **Table 1** and are accompanied by reliability indices to judge the fitting quality. These indices are weighted R (R_{wp}), the reduced chi-squared (χ^2), and R_e, which are related just to the profile of the XRD patterns, and R_p, which is related to the crystal structure. The reduced chi-squared is defined as $(R_{wp}/R_e)^2$, where R_{wp} is the index that should be analyzed to verify if the refinement is converging and R_e is the expected statistical value for R_{wp}.[23]

Table 1. Structural parameters and standard Rietveld agreement factors for SR-XRD patterns of 1wt% Pd/GDC and 1wt% Pd/PrDC samples taken at room temperature in air.

Sample	*a* (Å)	R_p	R_{wp}	R_e	χ^2
Pd/GDC	5.4192 (6)	3.36	4.18	2.56	2.73
Pd/PrDC	5.4197(6)	2.77	3.59	2.40	2.22

In **Table 2**, average crystallite size (D_{XRD}), specific surface area (SSA) and the primary particle size (d_{BET}), calculated from the BET data, are summarized for all samples after calcination at 500 °C. Both Pd-loaded nanocatalysts had similar SSA values, which were slightly lower than those of pure GDC and PrDC (57.2 and 60.2 $m^2.g^{-1}$, respectively). [20] The d_{BET}/D_{XRD} ratio in both spheres was 1.6, indicating that the crystallites exhibited a low degree of agglomeration. These results indicate that the thermal treatment used to impregnate the Pd did not strongly affect the spherical morphology, the crystallite size or the SSA of these materials.

Table 2- Average crystallite size (D_{XRD}), specific surface area (SSA) and calculated primary particle size (d_{BET}) for nanostructured 1 wt% Pd/GDC and 1 wt% Pd/PrDC spheres.

Sample	D_{XRD} / nm	SSA / $m^2.g^{-1}$	d_{BET} / nm	d_{BET}/D_{XRD}
Pd/GDC	9.7	54.9	15.5	1.6
Pd/PrDC	10.4	53.7	16.3	1.6

From SR-XRD data collected at 500 °C under reducing (5%H_2/He) and oxidizing (21%O_2/N_2) conditions, the lattice parameters were refined assuming a cubic phase (*Fm*3*m* space group) by the Rietveld method with the same assumptions as used for data obtained at room temperature. Moreover, for the case of the reducing atmosphere, a second phase corresponding to Pd (space group Fm3m with Pd^0 in the 4a position, according to ICDS#41517), was included. The results of Rietveld refinement of this SR-XRD data are summarized in **Table 3 (**and Electronic Supplementary Information, **Figure S3** and **S4**).

When the samples were heated from room temperature to 500 °C under reducing conditions (5%H_2/He), the lattice parameters increased in all samples, both due to the thermal expansion of the unit cell and the partial reduction of Ce and Pr in the solid solutions. On switching to oxidizing conditions (synthetic air) at 500 °C, the lattice parameters were seen to decrease for all samples, but to different extents. Clearly, the unit cell parameter is strongly dependent on the concentration of the cation dopant as well as on the gas atmosphere and temperature. However, no substantial differences can be

View Article Online
DOI: 10.1039/C8TA02031J

observed between lattice parameters obtained under the same conditions for LnDC and 1wt% Pd/LnDC (see Electronic Supplementary Information, **Table S1** and **S2**). [20]

Table 3. Structural parameters and standard Rietveld agreement factors for SR-XRD patterns of 1 wt% Pd/GDC and 1 wt% Pd/PrDC samples taken at 500 °C under reducing and oxidizing conditions.

Sample	Atmosphere	a (Å)	R_p	R_{wp}	R_e	χ^2
Pd/GDC	5%H_2/He	5.4514(5)	3.18	3.88	2.44	2.53
	21%O_2/N_2	5.4416(7)	3.03	3.68	2.49	2.19
Pd/PrDC	5%H_2/He	5.4667(5)	3.27	4.09	2.34	3.05
	21%O_2/N_2	5.4457(8)	3.32	4.13	2.4	2.95

Figure 7, shows an expanded area of the SR-XRD patterns in which the Pd(111) and PdO(111 and 200) reflections are clear. Under reducing conditions, the main peak of metallic Pd is clearly observed in 1wt% Pd/GDC and 1 wt% Pd/PrDC samples (**Fig 7a**). On the other hand, under oxidizing conditions at 500 °C, the main peaks of PdO alone were observed in both samples (**Fig 7b,** and Electronic Supplementary Information, **Figure S6** and **S7**) showing clearly that the metallic Pd was reoxidised. These results indicate that, at this temperature and in these samples, palladium changes easily from Pd^0 under reducing conditions to Pd^{II} under oxidizing conditions.

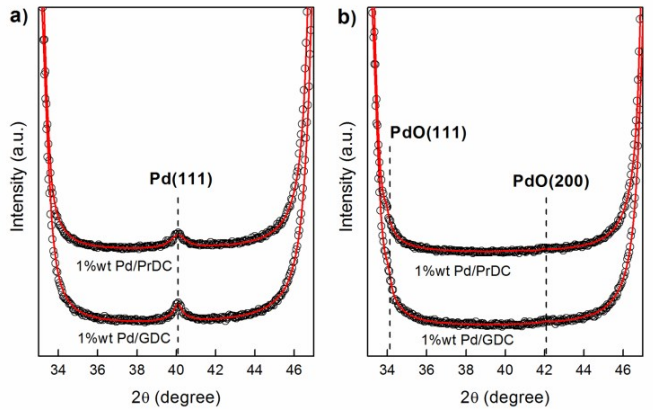

Figure 7. Synchrotron HT-XRD patterns of 1 wt% Pd/GDC and 1 wt% Pd/PrDC samples in the vicinity of the Pd (111), PdO (111) and PdO (200) peaks at 500 °C under a) reducing and b) oxidizing conditions.

Normalized Ce L_3-edge XANES spectra for the nanostructured 1 wt% Pd/GDC and 1 wt% Pd/PrDC spheres obtained at 500 °C under reducing and oxidizing conditions, are presented in **Figure 8**. These exhibit two clear peaks frequently labelled A and B. Peak A is assigned as a Ce^{4+} peak with the final state $2p^54f^05d^1$, which denotes that an electron is excited from the Ce 2p shell to its 5d shell, with no electron in the 4f shell. Peak B is also a Ce^{4+} peak, with the final state $2p^54f^15d^1v$, which denotes that in addition to an electron excited from the Ce 2p shell to the 5d shell, another electron is also excited from the valence band (O 2p shell) to the Ce 4f shell, leaving a hole (v) in the valence band. Some authors refer to Peak C as a Ce^{3+} peak.[24] An additional small peak (D) is present at pre-edge and likely arises from transitions to the bottom of the conduction band. The Ce L_3-absorption edges for all samples are close to 5725.7 eV (values were determined from the first and second derivatives of the Ce L_3-edge XANES spectra for each sample).

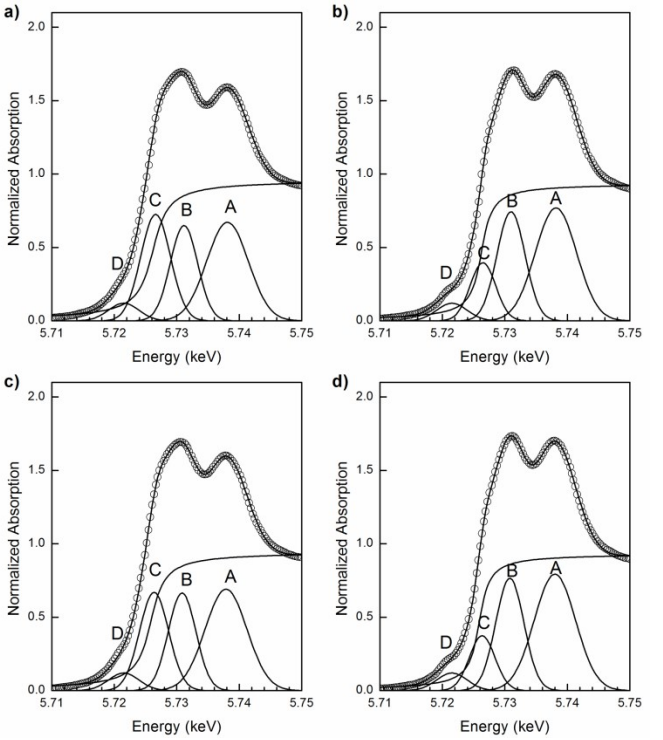

Figure 8. Normalized Ce L_3-edge XANES spectra for 1 wt% Pd/GDC obtained at 500 °C in (a) reducing and (b) oxidizing conditions; and 1 wt% Pd/PrDC obtained at 500 °C in (c) reducing and (d) oxidizing conditions, showing the experimental data (empty circles), four Gaussian peaks (A-D), and one arctangent function obtained by least-squares fitting and the sum of all five functions (continuous black lines).

Data analysis was conducted by least-squares fitting four Gaussian profiles and one arctangent function to the experimental XANES data in the range between 5710 and 5750 eV. The ratio between the area of peak C (associated with Ce^{3+}) and the sum of the areas of peaks A, B and C (A and B are associated with Ce^{4+}) gives direct information about the fraction of Ce present as Ce^{3+}.[19] All values were normalized to the fraction of Ce present as Ce^{3+} in pure CeO_2 at room temperature. In both samples (**Table 4**), in air, no large differences were observed in the fractions of $Ce^{3+}/(Ce^{4+}+Ce^{3+})$ between room temperature and 500 °C. In contrast, under reducing conditions at 500 °C, peak C (Figure 8) is clearly larger - and the percentage of Ce^{3+} calculated is dramatically higher - than in air at the same temperature.

The negative values in **Table 4** simply indicate that the Ce^{3+} content of the 1 wt% Pd/PrDC samples is lower than in the reference material, pure, undoped CeO_2. As expected, in both Gd- and Pr-doped samples, only small amounts of Ce^{3+} are

View Article Online
DOI: 10.1039/C8TA00285C

seen in the oxidizing environment (both at room temperature and 500 °C) and these levels increase considerably on exposing the samples to H_2 at 500 °C. In a previous study, an increase in reducibility on doping pure ceria with Gd or Pr (so introducing oxygen ion vacancies) was observed, with a Ce^{3+} content of 7.3 and 8.4% for GDC and PrDC, respectively.[20] A significant increase in reducibility caused by the incorporation of Pd was observed in the present work for 1 wt% Pd/GDC (17.3%) and 1wt% Pd/PrDC (15.0%). Two mechanisms for reduction of the Ce are possible. The first one would involve the direct adsorption of H_2 on the oxide, followed by reaction and release of water. The second would involve reduction of PdO to Pd with subsequent adsorption of H_2 on the Pd and spillover of H species onto the oxide surface, where these could reduce the oxide and again form water. Evidence of facile reduction of PdO to Pd is given in the SR-XRD data in **Figure 7 a** and **b** and spillover of hydrogen from Pd nanoparticles is known to occur easily, even at low temperatures.[25-27] Therefore, reduction via spillover from the (reduced) Pd nanoparticles is likely to dominate over direct reduction of the oxide. This explains the increase in reducibility on going from LnDC to 1wt% Pd/LnDC materials.

Table 4. Fraction of Ce present as Ce^{3+} in 1 wt% Pd/GDC and 1 wt% Pd/PrDC samples at 25 °C in air and under reducing and oxidizing conditions at 500 °C, estimated from fittings to the Ce L_3-edge XANES spectra.

Sample	Temperature (°C)	Atmosphere	$Ce^{3+}/(Ce^{4+}+Ce^{3+})$ %
Pd/GDC	25	21% O_2/N_2	0.5
	500	5% H_2/He	17.3
	500	21% O_2/N_2	0.4
Pd/PrDC	25	21% O_2/N_2	0.6
	500	5% H_2/He	15.0
	500	21% O_2/N_2	-0.7

Fig. 9 presents the normalized XANES spectra at the Pr L_3-edge obtained at 500 °C under reducing (5%H_2/He, 20 mL.min^{-1}) and subsequent oxidizing (synthetic air: 21% O_2/N_2, 50 ml.min^{-1}) conditions. At first sight, it could be assumed that the extent of re-oxidation (seen as the Pr^{3+} switching to Pr^{4+} in oxidizing atmospheres) of these samples is rather low, since the white line assigned to Pr^{4+} is rather small. However, there are studies that show that even in XANES spectra of samples containing (nominally) 100% of the Pr in the +4 state, the white line for Pr^{4+} is not so pronounced, and that the presence of any peak should be taken as indicative of significant Pr^{4+} content.[28] Hence, our samples show significant levels of both Pr^{3+} and Pr^{4+} at 500 °C in oxidizing conditions. On the other hand, the spectra obtained under reducing conditions show that the Pr is completely reduced to Pr^{3+}. This is in agreement with the *in situ* SR-XRD results, where the moderate increase in lattice parameter can be ascribed to the increase in concentration of both Pr^{3+} and the related oxygen vacancies. The reduction of Ce^{4+} also contributes to a lesser extent to this unit cell expansion. As the authors previously showed in a study of another multivalent rare earth oxide, Ce^{3+} content is not independent of Pr^{3+} content, but they are related to the maximum number of oxygen vacancies allowed for the structure.[20,29]

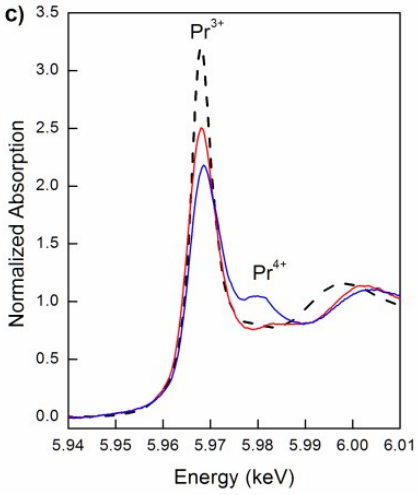

Figure 9. Normalized Pr-L_3 edge XANES spectra obtained at 500 °C under reducing (red line) and oxidizing (blue line) conditions. Spectra at room temperature for $Pr(NO_3)_3$ (Pr^{3+}; dotted line) is included for comparison in (c).

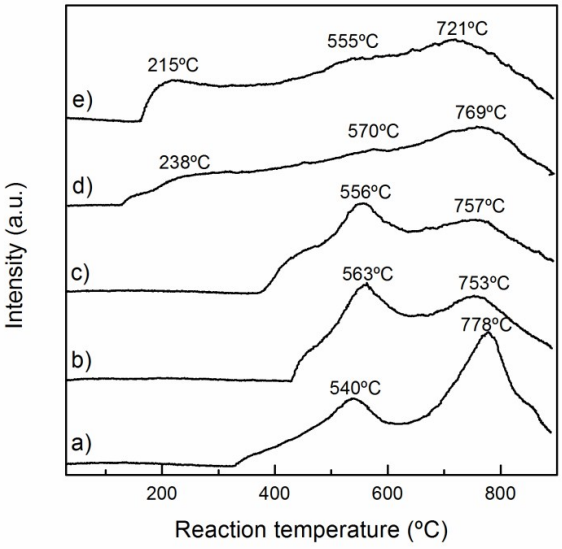

Figure 10. H_2-TPR profiles of a) CeO2, b) GDC, c) PrDC, d) 1 wt% Pd/GDC and e) 1 wt% Pd/PrDC.

The profiles of H_2O formation (m/e=18) in the H_2-TPR experiments are shown in **Figure 10**. Two broad peaks are observed at 540-563 and 757-778 °C for CeO_2 and LnDC (**Figure 10 a, b** and **c**). These can be attributed to the reduction of Ce^{4+} to Ce^{3+} on the surface and in the bulk of these materials, respectively. [30-32] In the traces for 1 wt% Pd/GDC (**Figure 10 d**) and 1 wt% Pd/PrDC (**Figure 10 e**), these two peaks were also observed. However, at 215-238 °C a further peak is clearly

View Article Online
DOI: 10.1039/C8TA00203G

observed. Since the reduction of the support materials, in the absence of Pd, starts at much higher temperatures (above 380 °C for GDC and PrDC), this reduction peak can be assigned to the reduction of PdO to Pd. However, it is well known that noble metals such as Pd can promote (via hydrogen spillover) the reduction of the support. Therefore, some contribution to these peaks from such Pd-promoted reduction of the support - once enough metallic Pd is present- cannot be discounted. Indeed, the "bridges" seen in the TPR spectra between the initial peaks at 215/238°C and those expected for the support materials (from 380°C upwards) are likely to be largely due to this process because the PdO particles, being so small, would be expected to be reduced quickly [15].

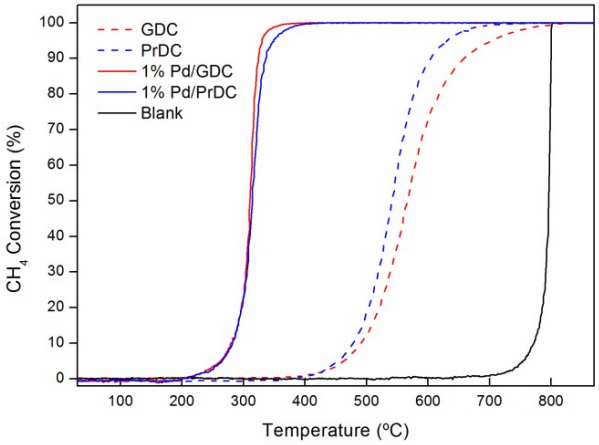

Figure 11. Catalytic activities of CH_4 combustion for 1 wt% Pd/GDC (red) and 1 wt% Pd/PrDC (blue) spherical nanocatalysts as a function of temperature. Nanostructured GDC (dotted red) and PrDC (dotted blue) spheres and non-catalytic sample (blank) are included for comparison.

In order to compare their catalytic activity, several tests were performed on the LnDC and 1 wt% Pd/LnDC spherical nanocatalysts, as explained in the experimental section. For comparison, a blank test was carried out using SiC only. In **Figure 11**, CH_4 conversion versus temperature for the different catalyst samples is plotted. In addition, T_{10}, T_{50} and T_{90} values were estimated from the experimental curves and are given in **Table 5**.

The catalytic activity of the bare supports was significantly better than that obtained in the blank test, and PrDC performed slightly better than GDC. The addition of Pd dramatically increased the activity of both samples, although the effect of the support dopant is very small. The temperature at which 50% conversion of CH_4 was reached (T_{50}) was used as an index of catalytic activity. The blank test exhibited the highest value of T_{50} (800 ºC). The 1 wt% Pd/GDC and 1 wt% Pd/PrDC samples exhibited very similar behaviour, and gave the lowest values of T_{50} (about 310 ºC) and, therefore, were by far the most active catalysts under these conditions. The improvement in T_{50} caused by impregnation of the LnDC by 1 wt% Pd is remarkable, the decrease in T_{50} being about 250 ºC.

Table 5. Temperature at which 10, 50 and 90% conversion of CH_4 was reached (T_{10}, T_{50} and T_{90}, respectively), estimated from the experimental curves (**Figure 11**). The values for 1 wt% Pd/GDC and 1 wt% Pd/PrDC correspond to for the 1st and 4th cycle.

Sample	T_{10} (ºC)	T_{50} (ºC)	T_{90} (ºC)
Blank	772	800	801
GDC	490	570	659
PrDC	478	530	604
1 wt% Pd/GDC (1st)	282	310	324
1 wt% Pd/GDC (4th)	310	355	446
1 wt% Pd/PrDC (1st)	282	310	336
1 wt% Pd/PrDC (4th)	320	367	337

The reaction rates at 300 ºC was estimated from Eq. 1 for the 1 wt% Pd/GDC and 1 wt% Pd/PrDC samples, as well as for some previous results reported by the authors in the literature, performed under the same conditions of the present work [19]. The comparison indicates that the samples studied in the present work show the highest reaction rate per palladium atom (about 29 mmols.g_{Pd}^{-1}.min^{-1}) in comparison with the other palladium-based catalysts (about 7 mmols.g_{Pd}^{-1}.min^{-1}) (see Electronic Supplementary Information, **Table S3 and Figure S8**). Here it is important to note that it is not possible to compare directly with other palladium-based catalysts because the experiments were carried out under different conditions. [16,17]

The fact that the spherical support particles are composed of nanoparticles of doped cerias containing one (Ce^{4+}/Ce^{3+}) or two (Ce^{4+}/Ce^{3+}, Pr^{4+}/Pr^{3+}) accessible redox couples and a high oxygen vacancy concentration is very likely to significantly increase the rate of transport of oxygen to the active sites in these catalysts and so improve their activity for oxidation reactions, as is seen in the data described above. The addition of the Pd function further dramatically increases catalytic activity. Dual-site mechanisms, where the nanoparticle-support interface plays a crucial role in activating the reactants, are commonly accepted to be important in the oxidation of methane over catalysts containing noble metals supported on reducible oxides.[33] In the catalysts of the present work, the interactions between the Pd-rich phase and the support are likely to be important because of the intimate relationship between the well-dispersed nanoparticles of the Pd-rich phase and the nanoparticulate support. This may explain the high catalytic activity observed. Unfortunately, the thickness and porosity of the spherical support particles make it impossible to carry out a full analysis of the size of the Pd-rich nanoparticles or of the nature of the metal-support interface. However, from the microscopy and other data presented here, it is expected that the microstructure of the support is such that it facilitates the dispersion of the Pd-rich phase in the form of nanoparticles, and therefore increases the total area of the interface between the active phase and the support, as well as the total length of the boundary between Pd-rich phase, ceria-based support and the reactants

in the gas phase (i.e. the nanoparticle edges). Either or both of these phenomena may be important in explaining the excellent catalytic activity observed here.

Results of cyclic catalytic stability experiments performed on 1 wt% Pd/LnDC spherical nanocatalysts show a deactivation after four cycles (see Electronic Supplementary Information, **Figure S9** and **S10**). From the first to the fourth cycles, the values of T_{50} increased from 310 °C to 355 °C for 1 wt% Pd/GDC and from 310 °C to 367 °C for 1 wt% Pd/PrDC (**Table 5** and Electronic Supplementary Information **Table S5** and **S6**).

The most likely causes of catalyst deactivation are obstruction or modification of active sites because of coke deposition, modification of the oxidation state of the Pd under the specific reaction conditions used and the thermal sintering - and loss of specific surface area - of the Pd-rich particles. Because of the large oxygen excess used in these experiments, it is very unlikely that the catalysts suffer deactivation or poisoning by carbon deposits. In addition, a temperature programmed oxidation experiment was carried out after the 4th cycle and a negligible amount of CO_2 was produced. Reduction of palladium oxide can be achieved even at high concentrations of oxygen, but at higher temperatures than those employed here.[16] Even though it was no possible to completely characterize the size and morphology of the Pd-rich nanoparticles, it is reasonable to assume that the activity loss is related to the sintering of the Pd-rich nanoparticles and possibly also to changes in their morphology that would affect the metal-support interaction and the chemical environment of the superficial Pd atoms.

It is well known that ceria-based mixed oxides act as oxygen storage materials, or oxygen buffers, in oxidation reactions because of the accessible Ce^{3+}/Ce^{4+} redox couple. Reduction of Ce^{4+} to Ce^{3+} is accompanied by loss of oxygen from the oxide, which can be used in the reaction. It is commonly accepted that ceria-based materials follow the Mars Van Krevelen mechanism in which the catalyst acts as the oxygen donor towards the reactant and this oxygen is replenished from the oxygen present in the gas phase and which thus acts as an indirect reactant, so keeping the catalyst in its oxidised, active form.[34] In the present work, the catalytic tests were carried out in excess oxygen, so this mechanism was favoured.

In pure GDC, Gd^{3+} ions introduce extrinsic oxygen vacancies, which in turn diminish the Ce^{3+} content in the material from a simple equilibrium point of view.[35] The GDC then shows a higher Ce^{4+} content than pure ceria (under the same external conditions), and, it is proposed that, as a consequence, it displays higher catalytic activity. The higher oxygen vacancy concentration would also tend to allow faster loss and uptake of oxygen from the gas phase, so improving the redox kinetics. T_{50} data for pure ceria and pure GDC were reported in a previous study. [19]

In Pd-containing materials, the exact catalytic mechanism for hydrocarbon oxidation is not fully understood, and neither are the species that are involved. Nevertheless, there is a general consensus that the active phase is probably PdO or an equivalent intermediate, but that metallic Pd shows worse or no catalytic activity at all.[36-38] There is also evidence for an enhancement effect conferred by ceria-related materials on the PdO active phase and hence on the catalytic activity.[39,40] Even in the case of catalytic tests using unsupported Pd, it has been shown that the active phase for hydrocarbon oxidation is PdO and not metallic Pd.[41]

In order to further understand the physicochemical properties of these catalysts and the catalytic mechanism, a future detailed study using theoretical ab initio density functional theory (DFT+U) calculations is planned by the authors. The chemical and structural properties of active sites on the Pd–ceria surface are difficult to characterize, especially under reaction conditions. Strong interactions between palladium and the ceria support may stabilize oxidized $Pd^{\delta+}$ species, which may contribute to the significant activity of Pd/ceria based materials for methane oxidation. Of special interest is the question of whether calculations from first principles predict the presence of oxygen vacancies under the reaction conditions employed in this study and, if so, where they are located. This is a very important issue since oxygen vacancies play a central role in the transport properties within these materials during redox reactions.

Conclusions

In the present work, nanostructured $Ce_{0.9}Gd_{0.1}O_{2-\delta}$ (GDC) and $Ce_{0.9}Pr_{0.1}O_{2-\delta}$ (PrDC) spheres previously obtained by microwave assisted hydrothermal homogeneous co-precipitation were impregnated with 1 wt% Pd by the incipient wetness impregnation of an aqueous Pd^{2+} solution. Their properties were characterized by synchrotron radiation X-ray diffraction (SR-XRD), X-ray absorption near-edge spectroscopy (XANES) and scanning and high resolution electron microscopy with X-ray spectroscopy.

The addition of 1 wt% Pd to the LnDC dramatically increased the reducibility of the Ce in the mixed oxide. This was demonstrated by analysis of in situ XANES spectra obtained under reducing conditions. Clearly, the Pd improves the Ce^{3+}/Ce^{4+} redox couple in LnDC materials.

High activity for CH_4 oxidation was observed in nanostructured 1 wt% Pd/LnDC spheres with total conversion of CH_4 attained at a temperature below 400 °C.

These findings open up an interesting avenue for future work in this area, and indicate great promise for application of these particular catalyst systems.

Acknowledgements

This work has been supported by: the Brazilian Synchrotron Light Laboratory (LNLS, Brazil), under proposals D04B-XAFS1-13435 and D12A-XRD1-13437; Chinese Scholarship Council (CSC, China); and Agencia Nacional de Promoción Científica y Tecnológica (Argentina, PICT 2012-1506). Electron Microscopy was performed at the Electron Microscopy Facility, University of St Andrews. The authors are grateful to Fernando Muñoz, Anna Paula da Silva Sotero Levinsky, Cristiane Rodella, Fábio Zambello, Tamiris Bouças Piva and Simone Baú Betim for their

invaluable experimental assistance at the LNLS and Gabriela Numma for figures and graphics design. Dr. L.M. Acuña and Dr. R.O. Fuentes are members of CIC-CONICET, Argentina. Dr. J. J. Delgado thanks the "Ramón y Cajal" program of the Ministry of Economy, Industry and Competitiveness of Spain. Dr. R.O. Fuentes gratefully acknowledges the UCA-International fellowship (UCA/R82REC/2016), Universidad de Cadiz, Spain.

References

1 R. Di Monte, J. Kaspar, Top. Catal., 2004, **28**, 47-57.
2 S.D. Park, J.M. Vohs, R.J. Gorte, Nature, 2000, **404**, 265-267.
3 S.M. Haile, Mater. Today, 2003, **6**, 24-29.
4 B.H.C. Steele, Nature, 1999, **400**, 619-621.
5 J. Kaspar, P. Fornasiero, in: A. Trovarelli (Ed), Catalysis by Ceria and Related Materials, Imperial College Press, London, 2002, pp 217-236.
6 J.A. Kilner, Solid State Ionics, 2000, **123**, 13-23.
7 B.C.H. Steele, Solid State Ionics, 2000, **129**, 95-110.
8 H.L. Tuller, S.R. Bishop, D. Chen, Y. Kuru, J.-J. Kim, T.S. Stefanik, Solid State Ionics, 2012, **225**, 194-197.
9 A.A. Yaremchenko, A.A. Valente, V.V. Kharton, I.A. Bashmakov, J. Rocha, F.M.B. Marques, Catal. Commun., 2003, **4**, 477-483.
10 S.P. Jiang, X.J. Chen, S.H. Chan, J.T. Kwok, J. Electrochem. Soc., 2006, **153** 5, A850-A856.
11 R.T. Baker, I.S. Metcalfe, P.H. Middleton, B.C.H Steele, Solid State Ionics, 1994, **72**, 328-333.
12 R.T. Baker, I.S. Metcalfe, Appl. Catal. A, 1995, **126**, 297-317.
13 R.T. Baker, I.S. Metcalfe, Appl. Catal.A, 1995, **126**, 319-332.
14 S. Tao, J.T.S. Irvine, S.M. Plint. J. Phys. Chem B, 2006, **110**, 21771-21776.
15 K. Wu, L-D. Sun, C-H. Yan, Adv. Energy Mater., 2016, **6**,1-7.
16 M. Cargnello, J.J. Delgado Jaén, J.C. Hernández Garrido, K. Bakhmutsky, T. Montini, J.J. Calvino Gámez, R.J. Gorte, P. Fornasiero, Science, 2012, **337**, 713-717.
17 S. Xie, Y. Liu, J. Deng, X. Zhao, J. Yang, K. Zhang, Z. Han, H. Dai, Journal of Catalysis, 2016, **342**, 17–26.
18 F.F. Muñoz, M.D. Cabezas, L.M. Acuña, A.G. Leyva, R.T. Baker, R.O. Fuentes, J. Phys. Chem. C, 2011, **115**, 19687-19696.
19 F.F. Muñoz, R.T. Baker, A.G. Leyva, R.O. Fuentes, Appl. Catal. B: Environmental, 2013, **136-137**, 122-132.
20 F.F. Muñoz, L.M. Acuña, C. Albornoz, A.G. Leyva, R.T. Baker, R.O. Fuentes, Nanoscale, 2015, **7**, 271-281.
21 H. Klug, L. Alexander, in: X-ray Diffraction Procedures for Polycrystalline and Amorphous Materials, John Wiley, New York, 1974, pp. 618.
22 J. Rodríguez-Carvajal, FullProf Suite Program, Version 2.05. Laboratoire León Brillouin. Saclay, France: CEA-CNRS; 2011.
23 R.A. Young, in The Rietveld Method, R.A. Young (Ed), Oxford University Press, Oxford, 1993, Chapter 1, pp. 21-24.
24 F. Zhang, P. Wang, J. Koberstein, S. Khalid, S-W. Chan, Surf. Sci., 2004, **563**, 74-82.
25 J.M. Gatica, R.T. Baker, P. Fornasiero, S.; Bernal, J. Kašpar, J. Phys. Chem. B, 2001, **105**, 1191-1199.
26 A. Norman, V. Perrichon, Phys. Chem. Chem. Phys., 2003, **5**, 3557-3564.
27 F.C. Gennari, A. Carbajal Ramos, A. Condó, T. Montini, S. Bengió, A. Cortesi, J.J. Andrade Gamboa, P. Fornasiero, Appl. Catal. A, 2011, **398**, 123-133.
28 I. A. Sluchinskaya, A. I. Lebedev, A. Erko, Phys. Solid State, 2012, **54** 5, 975–979.
29 L.M. Acuña, F.F. Muñoz, C. Albornoz, A.G. Leyva, R.T. Baker, R.O. Fuentes, J. Mater. Chem. A, 2015, **3**, 16120–16131.
30 J. Kaspar, P. Fornasiero, M. Graziani, Catal. Today, 1999, **50**, 285-298.
31 Y. Zuo, X. Huang, L. Li, G. Li, J. Mater. Chem. A, 2013, **1**, 374-380.
32 L. Jiang, S. Fernández-García, M. Tinoco, Z. Yan, Q. Xue, G. Blanco, J.J. Calvino, A.B. Hungría, X. Chen, ACS Appl. Mater. Interfaces, 2017, **9** 22, 18595–18608.
33 I. X. Green, W. Tang, M. Neurock, J.T. Yates Jr., Science, 2011, **333**, 736-739.
34 J.L.G. Fierro, Metal Oxides Chemistry, Chapter 8, 2006, pp. 217.
35 U.; Hennings, R. Reimert, Appl. Catal. B, 2007, **70**, 498-508.
36 S. Colussi, A. Trovarelli, E. Vesselli, A. Baraldic, G. Comelli, G. Groppi, J. Llorca, Appl. Catal. A, 2010, **390**, 1–10.
37 S. Colussi, A. Trovarelli, G. Groppi, J. Llorca, Catal. Commun., 2007, **8**, 1263-1266.
38 A. Hellman, A. Resta, N.M. Martin, J. Gustafson, A. Trinchero, P.A. Carlsson, O. Balmes, R. Felici, R. van Rijn, J.W.M. Frenken, J.N. Andersen, E. Lundgren, H. Grönbeck, J. Phys. Chem. Lett., 2012, **3**, 678−682.
39 L.M.T. Simplício, S.T. Brandão, D. Domingos, F. Bozon-Verduraz, E.A. Sales, Appl. Catal. A, 2009, **360**, 2-7.
40 L. Meng, J-J. Lin, Z-Y. Pu, L-F. Luo, A-P. Jia, W-X. Huang, M-F. Luo, J-Q. Lu, Appl. Catal. B, 2012, **119**-12, 117-121.
41 B.G. Hoflund, H.A.E. Hagelin, J.F. Weaver, G.N. Salaita, Appl. Surf. Sci., 2003, **205**, 102-112.

View Article Online
DOI: 10.1039/C8TA00203G

Table of contents entry

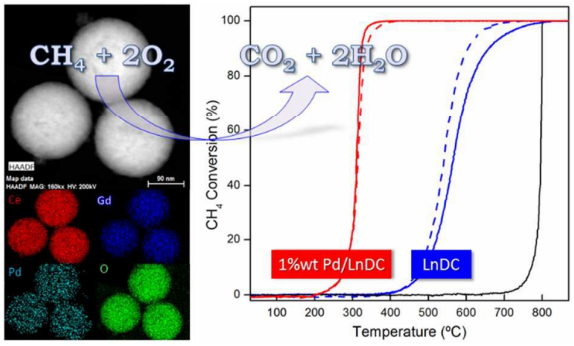

Nanostructrured 1 wt% Pd/LnDC spheres exhibited high activity for CH_4 oxidation with total conversion of CH_4 attained at a temperature below 400 ^{o}C.